Supplementary information

Ultrahigh energy fiber-shaped supercapacitors based on porous hollow conductive polymer composite fiber electrodes

Yangfan Zhang,[a] Xiyue Zhang,[a] Kang Yang,[a] Xuliang Fan,[a] Yexiang Tong,[a] Zishou Zhang,*[a] Xihong Lu,*[a] Kancheng Mai,[a] Qingqing Ni,[b] Mingqiu Zhang[a] and Xudong Chen[a]

[a] MOE of the Key Laboratory for Polymeric Composite and Functional Materials, MOE of the Key Laboratory of Bioinorganic and Synthetic Chemistry, Guangdong Provincial Key Laboratory for High Performance Resin-based Composites, Materials Science Institute, School of Chemistry, Sun Yat-sen University, Guangzhou 510275, China.
[b] Interdisciplinary Graduate School of Science and Technology, Shinshu University, Ueda, Japan.
E-mail: zhzish@mail.sysu.edu.cn, luxh6@mail.sysu.edu.cn

Calculations

The linear capacitance (C_L) and areal capacitance (C_A) of the individual fiber electrode PHCFs@PANI were calculated based on the following equations:

$$C_L = \frac{Q}{L \times \Delta V} \quad (1)$$

$$C_A = \frac{Q}{A \times \Delta V} \quad (2)$$

where Q (C) is the average electric quantity in the charge and discharge process of CV measurement, ΔV (V) is operating voltage window in the CV measurement, L (cm) is the length of the tested individual fiber electrode PHCFs@PANI, A (cm^2) is the superficial area of the tested individual fiber electrode PHCFs@PANI,which is equal to the circumference of cross section multiplied by the L.

The cell (device) capacitance (C_{cell}), linear capacitance (C_L) and areal capacitance (C_A) of the S-FSC devices were calculated from the slope of the discharge curve using the following equations:

$$C_{cell} = \frac{I \times \Delta t}{\Delta V} \quad (3)$$

$$C_L = \frac{C_{cell}}{L} = \frac{I \times \Delta t}{\Delta V \times L} \quad (4)$$

$$C_A = \frac{C_{cell}}{A} = \frac{I \times \Delta t}{\Delta V \times A} \quad (5)$$

where I (A) is the applied current, L (cm) is the length of overlapped portion of two fiber electrodes in the device, A (cm^2) is the superficial area of the whole device including the separator and encasement, which is equal to the circumference of cross section of the the whole device multiplied by the L, Δt *(s)* is the discharging time, ΔV *(V)* is the voltage window. Areal energy density, and power density of the devices were derived from the following equations:

$$E_A = \frac{1}{2 \times 3600} \times C_A \times \Delta V^2 \tag{6}$$

$$P_A = \frac{3600 \times E_A}{\Delta t} \tag{7}$$

where E_A ($mWh\ cm^{-2}$) is the energy density, C_A is the areal capacitance obtained from Equation (5), ΔV (V) is the voltage window, P_A ($W\ cm^{-2}$) is the power density, and Δt (s) is the discharging time.

Volumtric energy density and power density of the devices could be obtained from the following equations:

$$E_V = \frac{1}{2 \times 3600} \times \frac{C_{cell}}{V} \times \Delta V^2 \tag{8}$$

$$P_V = \frac{3600 \times E_V}{\Delta t} \tag{9}$$

where E_v ($mWh\ cm^{-3}$) is the energy density, C_{cell} is the cell capacitance obtained from Equation (3), V is the volume of the whole device including the separator and encasement, which is equal to the area of cross section multiplied by the L, ΔV (V) is the voltage window, P_A ($W\ cm^{-2}$) is the power density, and Δt (s) is the discharging time.

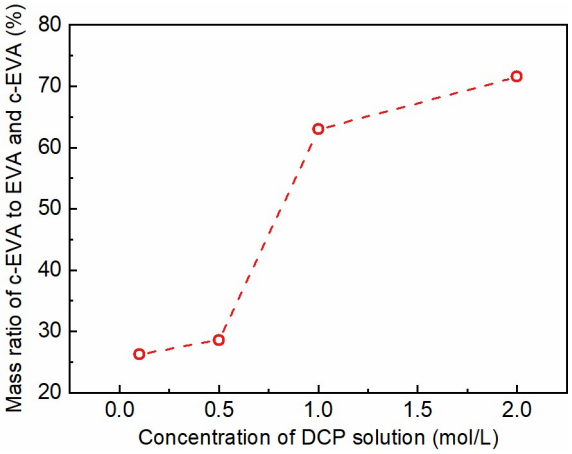

Figure S1. The mass ratio of c-EVA to EVA and c-EVA of the HCFs CNT/EVA/c-EVA as a function of concentration of DCP solution. When the concentration of DCP solution is lower than 0.1 mol/L, the hollow structrure of the PHF tended to collapse after removal of EVA. And when the concentration of DCP solution is higher than 2 mol/L, most EVA were crosslinked into c-EVA with only a small amount of EVA left, which results in few nanoporous formed in the PHCFs after removal of EVA. Thus, the relationship between the mass ratio of c-EVA to EVA and

c-EVA of the HCFs CNT/EVA/c-EVA and the concentration of DCP solution are available in the range of 0.1-2 mol/L. The mass ratio of c-EVA to EVA and c-EVA improved with the concentration of DCP solution increased. Apparently, the lowest concentration of DCP solution 0.1 mol/L used in the reaction contributed to remain the largest amount of EVA in the resultant HCFs CNT/EVA/c-EVA, which would lead to the largest pore volume and highest specific surface area for the PHCFs after removal of EVA. The pore volume and specific surface area of the HCFs and the PHCFs prepared with the concentration of DCP solution of 0.1, 0.5, 1.0 and 2.0 mol/L, respectively, are compared in Figure S2 below. Specifically, the PHCFs in this work are the ones prepared with the concentration of DCP solution of 0.1 mol/L.

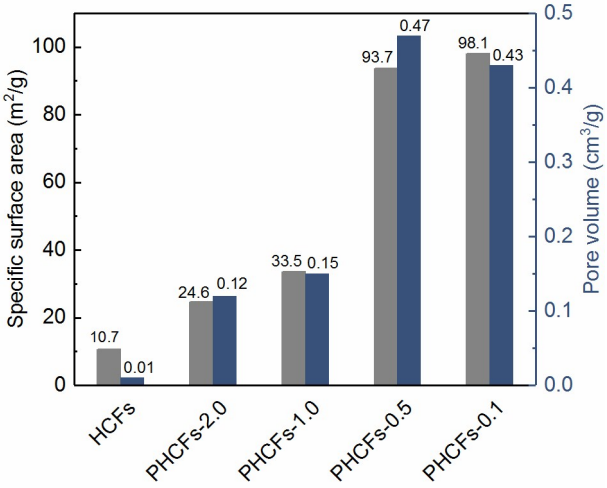

Figure S2. Comparison on the pore volume and specific surface area of the HCFs and the PHCFs prepared with the concentration of DCP solution of 0.1, 0.5, 1.0 and 2.0 mol/L.

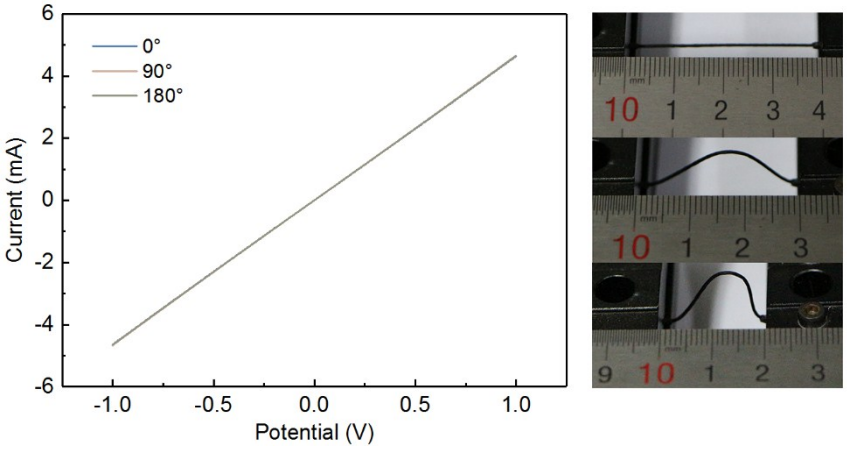

Figure S3. Linear sweep voltammograms (LSV) curves collected for the PHFs under various bending conditions (left) and the corresponding digital photos (right).

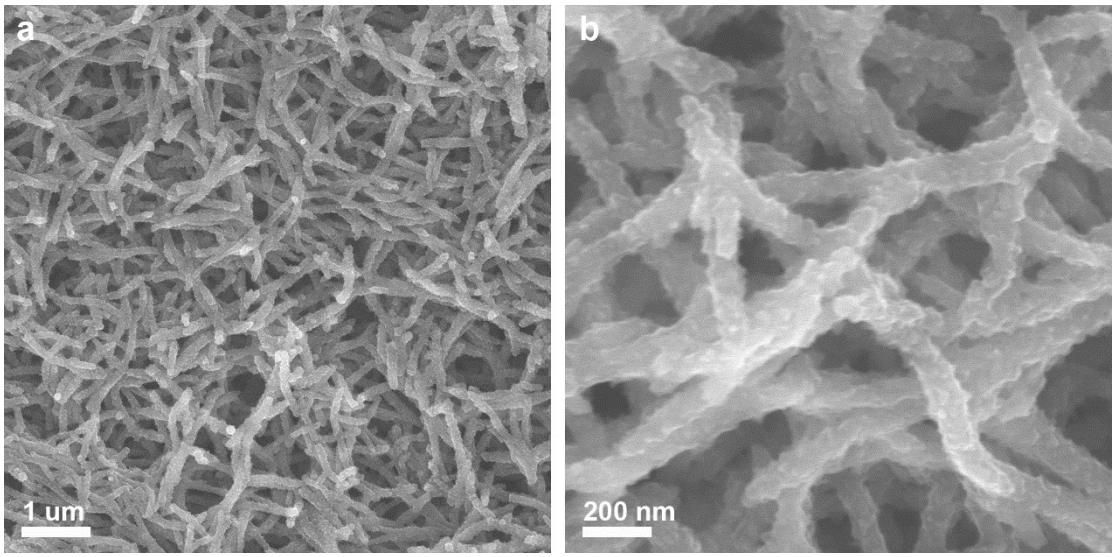

Figure S4. (a) Low-resolution and (b) high-resolution SEM image of PHCFs@PANI.

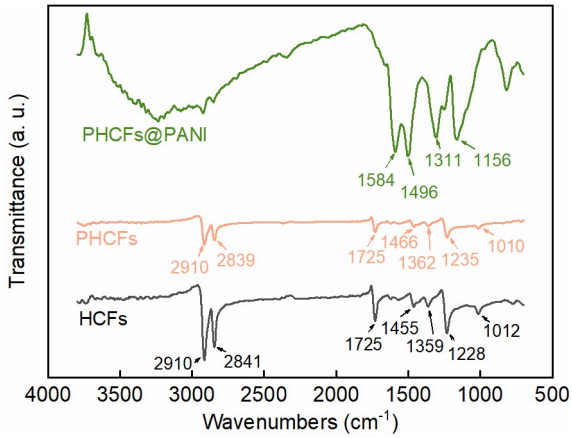

Figure S5. ATR-FTIR spectra of HCFs, PHCFs and PHCFs@PANI. Similar characteristic peaks were observed in the spectra of HCFs and PHCFs. The peaks at 2910 cm^{-1}, 2839 cm^{-1}, 1725 cm^{-1}, 1466 cm^{-1}, 1362 cm^{-1}, 1235 cm^{-1}, 1010 cm^{-1} were the characteristic absorptions of EVA, in which the peaks at 2910 cm^{-1} and 2839 cm^{-1} could be assigned to $-CH_2-$ or $-CH_3$ asymmetric and symmetric stretching vibration, the peaks at 1725 cm^{-1}, 1235 cm^{-1} and 1010 cm^{-1} were caused by C=O and C-O deformation vibration, the peaks at 1466 cm^{-1} and 1362 cm^{-1} could originate from asymmetric deformation vibration of $-CH_2-$ and $-CH_3$.[1] None of the obvious peaks could be ascribed to the characteristic absorptions of CNT due to the structural symmetry of CNT. The similar characteristic peaks observed for HCFs and PHCFs were consistent with the crosslinking mechanism mentioned in the manuscript, and the molecular chain structure of HCFs and PHCFs. For the spectra of PHCFs@PANI, the peak at 1584 cm^{-1} could be assigned to the stretching vibration of quinoid diimine unit C=C and C=N. While the characteristic peak ralated to the aromatic ring stretching of benzenoid unit C=C appeared at 1496 cm^{-1}. The peaks at 1311 cm^{-1} and 1156 cm^{-1} could originate from the secondary aromatic amine C-N stretching and the stretching of N=quinoid=N.[2] All those characteristic peaks of PANI indicated that PANI was grown in the PHCFs. The characteristic absorptions of EVA failed to detected in the spectra of PHCFs@PANI, which could be attributed to the use of ATR-FTIR.

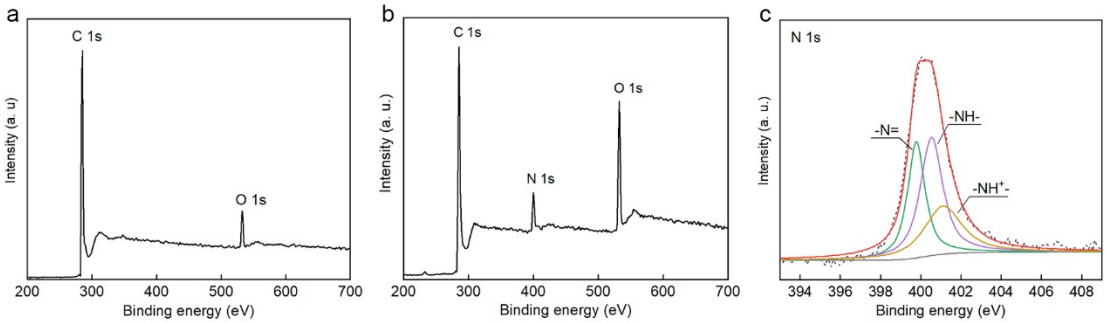

Figure S6. XPS survey spectra of (a) PHCFs and (b) PHCFs@PANI. (c) XPS N 1s spectra of PHCFs@PANI. Compared with XPS survey spectra of PHCFs, N 1s spectra appeared in the survey spectra of PHCFs@PANI, which might originate from PANI. The N 1s spectra could be deconvoluted into three peaks at 399.8 eV, 400.5 eV and 401.1 eV, which were assigned to the quinoid imine (-N=), the benzenoid amine (-NH-) and the positively charged nitrogen (-NH^+-), respectively.[3] It could be concluded that PANI was deposited on the PHCFs in the protonated emeraldine salt form.

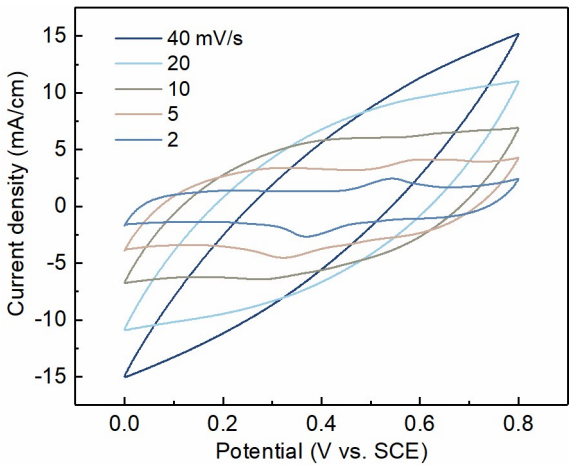

Figure S7. CV curves of PHCFs@PANI collected at the scan rate from 2 to 40 mV/s. A couple of redox peaks could be observed in the CV curve at the scan rate of 5 mV/s. The redox peaks were associated with the redox transition of PANI between leucoemeraldine form and polaronic emeraldine form, which contributed to the redox capacitance.[4] With the increase in scan rate from 10 to 40 mV/s, the redox peaks shifted from the original position to positive or negative direction and finally disappeared in the CV curves. This phenomenon might be explained by that the polarization effect became obvious with the scan rate increasing.[5]

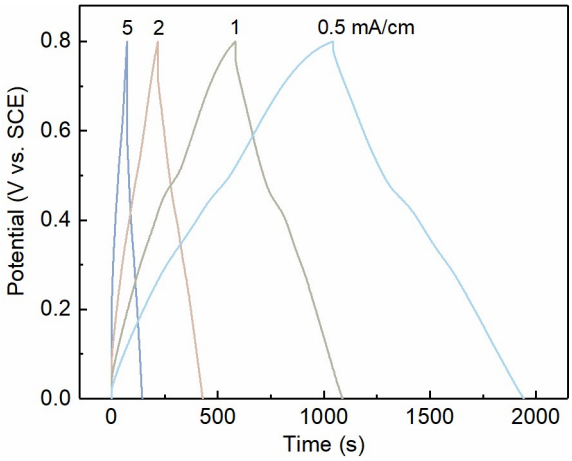

Figure S8. GCD curves of PHCFs@PANI collected at the current density from 0.5 to 5 mV/s.

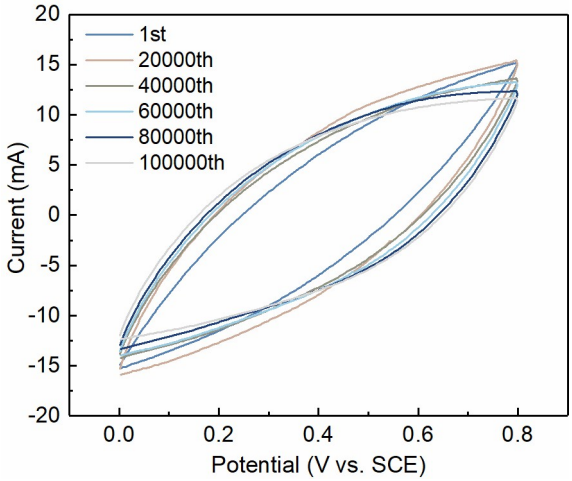

Figure S9. CV curves of PHCFs@PANI collected at the 1st, 20,000th, 40,000th, 60,000th, 80,000th and 100,000th cycle.

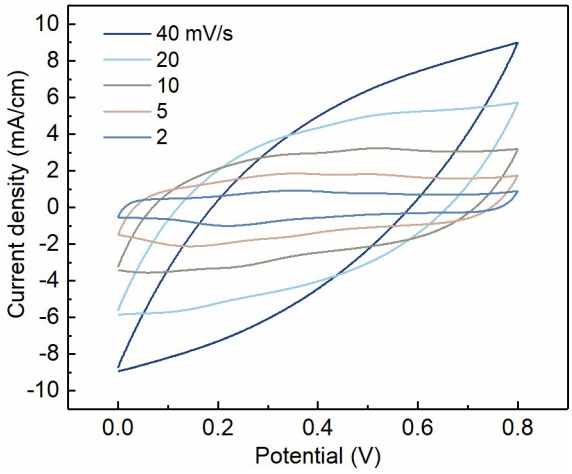

Figure S10. CV curves of the S-FSC device collected at the scan rate from 2 to 40 mV/s.

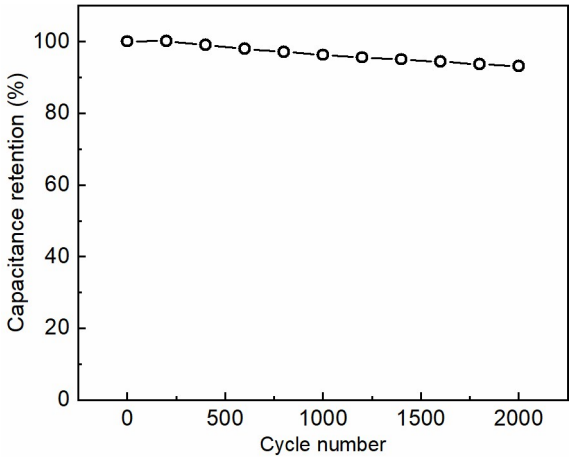

Figure S11. Cycle performance of the S-FSC device collected at the scan rate of 40 mV/s. The cycle stability of the S-FSC device was below expectation. The slight decrease in capacitance of the S-FSC could be ascribed to the sustained water evaporation from the PVA/H_2SO_4 gel electrolyte, resulting in the decrease in ionic conductivity of gel electrolyte and ion transport.

Table S1. Comparison on linear capacitance and areal capacitance between our PHCFs@PANI based S-FSC and other FSCs reported recently.

Electrode materials	Linear capacitance [mF/cm]	Areal capacitance [mF/cm^2]	Ref.
PHCFs@PANI	**278**	**622**	**This work**
Chinese ink/stainless steel wire	0.1	3.18	6
Fe_3O_4 nanosheet array/Fe wire	20.8	/	7
TiN@C nanotubes/Ti wire	2.4	19.4	8
rGO/Au wire	0.102	6.49	9
PEDOT/MWCNT yarn/Pt wire	0.46	73	10
ZnO nanowires/MnO_2/Au–PMMA wire	0.2	2.4	11
Pen ink/Au-plastic wire	0.504	19.5	12
rGO/SWCNT@CMC	5.3	177	13
Graphene hydrogenls/MWCNT/cotton thread	0.098	/	14
MWCNT/carbon fiber	6.3	86.8	15
SWCNT/activated carbon yarn	/	37.1	16
PANI nanopillars array/N-doped carbon nanofibers	85.1	123.2	17
CNT fiber	0.029	8.66	18
CNT fiber	0.006	/	19
CNT fiber	/	4.28	20
MnO_2/CNT fiber	0.015	3.01	19
Co_3O_4/CNT fiber	/	52.6	21
PANI/IR-CNT yarn	/	43	22
OMC/CNT yarn	1.91	39.7	23
rGO/CNT yarn	0.027	4.97	19

PANI nanowire array/CNT yarn	/	38	24
N-doped rGO/SWCNT fiber	/	116	25
rGO fiber	0.011	0.726	9
PPy/rGO fiber	/	107.2	26
Hollow rGO/PEDOT:PSS fiber	8.1	304.5	27
Graphene fiber@3D graphene	0.02	1.7	28
Graphene fiber	/	1.2	29
Graphene fiber	/	0.443	30
MnO2/graphene/Graphene fiber	/	9.6	31
PEDOT:PSS fiber	/	119	32
CNT@MnO2 fiber//CNT@PPy fiber	5.00	60.435	33
CNT@ZnO@MnO_2//CNT fiber	/	31.15	34
Ni(OH)2 nanowire fiber//ordered mesoporous carbon fiber	6.67	35.67	35

References

1 Y. Lei and B. Qu, *Polym. Degrad. Stabil.*, 2008, **93**, 918-924.

2 S. Wang, J. Shang, Q. Wang, W. Zhang, X. Wu, J. Chen, W. Zhang, S. Qiu, Y. Wang and X. Wang, *ACS Appl. Mat. Interfaces*, 2017, **9**, 43939-43949.

3 C. A. Amarnath, N. Venkatesan, M. Doble and S. N. Sawant, *J. Mater. Chem. B*, 2014, **2**, 5012-5019.

4 J. Yan, T. Wei, B. Shao, Z. Fan, W. Qian, M. Zhang and F. Wei, *Carbon*, 2010, **48**, 487-493.

5 Q. Li, J. Wu, Q. Tang, Z. Lan, P. Li, J. Lin and L. Fan, *Electrochem. Commun.*, 2008, **10**, 1299-1302.

6 D. Harrison, F. Qiu, J. Fyson, Y. Xu, P. Evans and D. Southee, *Phys. Chem. Chem. Phys.*, 2013, **15**, 12215-12219.

7 G. Li, R. Li and W. Zhou, *Nano-Micro Lett.*, 2017, **9**, 46.

8 P. Sun, R. Lin, Z. Wang, M. Qiu, Z. Chai, B. Zhang, H. Meng, S. Tan, C. Zhao and W. Mai, *Nano Energy*, 2017, **31**, 432-440.

9 Y. Li, K. Sheng, W. Yuan and G. Shi, *Chem. Commun.*, 2013, **49**, 291-293.

10 J. A. Lee, M. K. Shin, S. H. Kim, H. U. Cho, G. M. Spinks, G. G. Wallace, M. D. Lima, X. Lepró, M. E. Kozlov, R. H. Baughman and S. J. Kim, 2013, **4**, 1970.

11 J. Bae, M. K. Song, Y. J. Park, J. M. Kim, M. Liu and Z. L. Wang, *Angew. Chem. Int. Ed.*, 2011, **50**, 1683-1687.

12 Y. Fu, X. Cai, H. Wu, Z. Lv, S. Hou, M. Peng, X. Yu and D. Zou, *Adv. Mater.*, 2012, **24**, 5713-5718.
13 L. Kou, T. Huang, B. Zheng, Y. Han, X. Zhao, K. Gopalsamy, H. Sun and C. Gao, *Nat. Commun.*, 2014, **5**, 3754.
14 Q. Zhou, C. Jia, X. Ye, Z. Tang and Z. Wan, *J. Power Sources*, 2016, **327**, 365-373.
15 V. T. Le, H. Kim, A. Ghosh, J. Kim, J. Chang, Q. A. Vu, D. T. Pham, J.-H. Lee, S.-W. Kim and Y. H. Lee, *ACS Nano*, 2013, **7**, 5940-5947.
16 Q. Meng, H. Wu, Y. Meng, K. Xie, Z. Wei and Z. Guo, *Adv. Mater.*, 2014, **26**, 4100-4106.
17 D. Yang, W. Ni, J. Cheng, Z. Wang, C. Li, Y. Zhang and B. Wang, *Mater. Today Energy*, 2017, **5**, 196-204.
18 X. Chen, L. Qiu, J. Ren, G. Guan, H. Lin, Z. Zhang, P. Chen, Y. Wang and H. Peng, *Adv. Mater.*, 2013, **25**, 6436-6441.
19 J. Ren, L. Li, C. Chen, X. Chen, Z. Cai, L. Qiu, Y. Wang, X. Zhu and H. Peng, *Adv. Mater.*, 2013, **25**, 1155-1159.
20 P. Xu, T. Gu, Z. Cao, B. Wei, J. Yu, F. Li, J.-H. Byun, W. Lu, Q. Li and T.-W. Chou, *Adv. Energy Mater.*, 2014, **4**, 1300759-n/a.
21 F. Su, X. Lv and M. Miao, *Small*, 2015, **11**, 854-861.
22 F. Su, M. Miao, H. Niu and Z. Wei, *ACS Appl. Mater, Inter.*, 2014, **6**, 2553-2560.
23 J. Ren, W. Bai, G. Guan, Y. Zhang and H. Peng, *Adv. Mater.*, 2013, **25**, 5965-5970.
24 K. Wang, Q. Meng, Y. Zhang, Z. Wei and M. Miao, *Adv. Mater.*, 2013, **25**, 1494-1498.
25 D. Yu, K. Goh, H. Wang, L. Wei, W. Jiang, Q. Zhang, L. Dai and Y. Chen, *Nature Nanotech.*, 2014, **9**, 555-562.
26 X. Ding, Y. Zhao, C. Hu, Y. Hu, Z. Dong, N. Chen, Z. Zhang and L. Qu, *J. Mater. Chem. A*, 2014, **2**, 12355-12360.
27 G. Qu, J. Cheng, X. Li, D. Yuan, P. Chen, X. Chen, B. Wang and H. Peng, *Adv. Mater.*, 2016, **28**, 3646-3652.
28 Y. Meng, Y. Zhao, C. Hu, H. Cheng, Y. Hu, Z. Zhang, G. Shi and L. Qu, *Adv. Mater.*, 2013, **25**, 2326-2331.
29 Y. Hu, H. Cheng, F. Zhao, N. Chen, L. Jiang, Z. Feng and L. Qu, *Nanoscale*, 2014, **6**, 6448-6451.
30 J. Yu, M. Wang, P. Xu, S.-H. Cho, J. Suhr, K. Gong, L. Meng, Y. Huang, J.-H. Byun, Y. Oh, Y. Yan and T.-W. Chou, *Carbon*, 2017, **119**, 332-338.
31 Q. Chen, Y. Meng, C. Hu, Y. Zhao, H. Shao, N. Chen and L. Qu, *J. Power Sources*, 2014, **247**, 32-39.
32 D. Yuan, B. Li, J. Cheng, Q. Guan, Z. Wang, W. Ni, C. Li, H. Liu and B. Wang, *J. Mater. Chem. A*, 2016, **4**, 11616-11624.
33 J. Yu, W. Lu, J. P. Smith, K. S. Booksh, L. Meng, Y. Huang, Q. Li, J.-H. Byun, Y. Oh, Y. Yan and T.-W. Chou, *Adv. Energy Mater.*, 2017, **7**, 1600976-n/a.
34 Y. Li, X. Yan, X. Zheng, H. Si, M. Li, Y. Liu, Y. Sun, Y. Jiang and Y. Zhang, *J. Mater. Chem. A*, 2016, **4**, 17704-17710.
35 X. Dong, Z. Guo, Y. Song, M. Hou, J. Wang, Y. Wang and Y. Xia, *Adv. Funct. Mater.*, 2014, **24**, 3405-3412.